Check for updates

Active site exploration of core–corona structured bifunctional cobalt ferrite-containing nitrogen-doped carbon nanotubes for rechargeable zinc–air battery application†

Shankar Baskaran, E. A. Anook Nazer and Azhagumuthu Muthukrishnan [ID] *

First-row transition metal-containing bifunctional electrocatalysts are essential in developing metal–air batteries with high cycling efficiency. Core–corona structured porous N-doped carbon with tangled carbon nanotubes was synthesised by pyrolysing $CoFe_2O_4$ encapsulated ZIF-8. Structural characterisation indicates the presence of the CoFe metal alloy, which catalyses the formation of nanotubes. Besides, the CoFe alloy nanoparticles encapsulated by graphitic carbon improve the oxygen reduction and evolution reactions, corroborated by control samples. The bifunctional activity of the catalysts was analysed using the zinc–air battery, which exhibits an excellent power density of 162 mW cm^{-2} and a high specific capacity of 900 mA h g_{Zn}^{-1}. The real-time application was evaluated using the solid-state zinc–air battery, which exhibits the highest open circuit potential of 1.53 V. The CoFe alloy encapsulated N-doped carbon should be an efficient air-electrode catalyst for metal–air battery application.

Introduction

Rechargeable metal–air batteries have attracted much attention and are promising potential alternatives to the dominant Li-ion batteries in portable electronic devices. Zinc–air batteries (ZAB) are rapidly growing due to their high theoretical energy density and air-stable electrodes.[1–3] The development of low-cost and durable bifunctional electrocatalysts is one of the bottlenecks for the ZAB application in portable and wearable electronic devices. Although the combination of precious metals/metal oxides is used as catalysts, the development of electrocatalysts based on first-row transition metal elements is reported with higher efficiency.[4–6] Bifunctional activity of catalytic materials is preferred due to the two different reactions in ZABs, namely the oxygen evolution reaction (OER) and oxygen reduction reaction (ORR) during charging and discharging, respectively. First-row transition metal oxides,[7] chalcogenides,[8–10] nitrides,[11] metal alloys,[12] and bimetallic oxides (spinels and perovskites) can bring bifunctional activity.[13–17] Fe–N–C catalysts are well-developed for their ORR activity, whereas metal oxides are mostly known for their OER activity. Hence, bimetallic electrocatalysts are preferred as bifunctional catalysts in ZABs due to the different metal active sites for the ORR and OER.

School of Chemistry, Indian Institute of Science Education and Research Thiruvananthapuram, Maruthamala P.O., Vithura 695551, Kerala, India. E-mail: muthukrishnan@iisertvm.ac.in

† Electronic supplementary information (ESI) available. See DOI: https://doi.org/10.1039/d4se00084f

Bimetallic spinel oxides are widely studied for their ORR and OER activity and their applications in fuel cells and ZABs.[18–21] The presence of two metal ions in spinel oxides brought bifunctional catalytic activity (ORR and OER). Although several spinel compounds were reported for the ORR and OER activity, Co and Fe-based spinel materials are primarily known.[15,22,23] It may be attributed to the two metal active sites Fe and Co responsible for ORR and OER activity, respectively.[23] Besides, the activity can be improved by oxygen vacancies in spinel oxides. Bimetallic alloys on carbon supports (synthesised using the typical heat-treatment method) improve the ORR activity. The CoFe alloy was reported for its enhanced bifunctional activity due to the synergistic effect of both metals.[15,24,25] The role of carbon supports along with the metal active sites is very important. Carbon supports help to improve the conductivity and stability of metal/metal-oxide nanoparticles. Porous carbon materials derived from zeolitic imidazolate metal–organic frameworks could be perfect N-doped carbon materials.[26–28] ZIF-8 is a single carbon and nitrogen source to synthesise N-doped carbon, and is more active than pure carbon supports. Further, the ZIF-8 material yields porous N-doped carbon, which helps to improve mass transport.[29–31] The CoFe alloy was synthesised on the ZIF, followed by pyrolysis which leads to the CoFe–N/C materials.

Co and Fe-containing bimetallic compounds yield promising bifunctional activity, reported in recent days. Due to the poor conductivity of spinel oxides, conductive carbon supports were used along with spinel oxides to ensure facile electron transfer.

$CoFe_2O_4$ carbon composites have been extensively studied as ORR electrocatalysts.[32] The $CoFe_2O_4$ on graphitic carbon nitride support exhibits an onset potential of 0.90 V (vs. RHE) towards the ORR.[33] Polypyrrole-based N-doped carbon nanotubes were used as carbon supports for $CoFe_2O_4$, which show excellent ORR activity.[34] Hollow-structured $CoFe–CoFe_2O_4$ supported by N-doped carbon demonstrated excellent bifunctional activity in the zin–air battery.[35] N-doped carbon nanotubes derived from the $g-C_3N_4$ encapsulated CoFe alloy show excellent ORR and OER activity in zinc–air batteries.[22] The carbon matrix obtained from MOFs upon carbonisation shows better electrical conductivity, high surface area and permanent porosity. The ZIF-8 MOF is specially used to synthesise porous N-doped carbon, wherein the pores are generated due to the evaporation of metallic zinc.[29] Though several materials were synthesised based on Co and Fe metal/metal oxides, the ambiguity in discerning the real active sites has been seen throughout the literature.

Herein, ZIF-8 encapsulated $CoFe_2O_4$ was pyrolysed to synthesise $CoFe_2O_4$/NC catalysts, wherein the $CoFe_2O_4$ partially reduced to CoFe alloy nanoparticles with the formation of a core–corona structured N-doped carbon nanotube spikes. The ORR and OER activities were found to be excellent. The CoFe–N/C materials exhibit excellent ORR activity compared with Fe–N/C or Co–N/C catalysts synthesised using the same procedure. Besides, the CoFe–N/C catalyst-coated carbon air electrode in the liquid ZAB exhibits excellent power density and specific capacity.

Methodology

The $CoFe_2O_4$ was synthesised by using the previous synthetic protocol.[36] Briefly, 0.3 mole of $Fe(NO_3)_3\cdot 9H_2O$ (98%, Merck, India) was added to the 0.15 mole aqueous solution of $Co(NO_3)_2\cdot 6H_2O$ (98%, Merck, India) with constant stirring (35 mL) followed by the addition of 3 M NaOH (97%, Spectrochem, India) until the solution pH became 11.5 with continuous stirring for 6 hours. The content was transferred to a Teflon autoclave and heated to 180 °C for 12 hours. The precipitate was washed with DI water, ethanol and acetone, centrifuged and dried at 80 °C overnight. A desired amount of $CoFe_2O_4$ (CF) was sonicated in 40 mL methanol, and 0.587 g of $Zn(NO_3)_2\cdot 6H_2O$ (98%, Avra Synthesis, India) was added. With this mixture, 1.298 g of 2-methyl imidazole (2-MIM) (98%, Avra Synthesis, India) methanolic solution was added and sonicated to maintain the uniform dispersion. The dispersion was kept for 21 hours without disturbance. A pale brownish precipitate of the $CoFe_2O_4$–ZIF-8 composite was obtained and dried at 60 °C in an oven. Thus-synthesised composites were pyrolysed at 900 °C under a N_2-atmosphere to synthesise $CoFe_2O_4$-containing porous N-doped carbon (CF–N/C, CF indicates $CoFe_2O_4$ and N/C referred the N-doped carbon). CF10–N/C4, CF25–N/C4 and CF50–N/C4 catalysts were synthesised using the above protocol (the numbers 10, 25 and 50 refer to the initial amount of $CoFe_2O_4$ taken in milligrams, and 4 refers to the pyrolysis time in hours). The CF10–N/C4 was washed with 0.1 M HCl to remove the free excess metal oxides to analyse the role of spinel oxide,

and it was referred to as CF10–N/C4–AW. The Fe_3O_4 and Co_3O_4 encapsulated ZIF-8 composites were synthesised individually using a similar protocol and were named F10–N/C4 (only Fe) and C10–N/C4 (only Co) and analysed for ORR activity to understand the role of individual oxides.

The ZIF-8 was synthesised as reported in the literature.[37] 0.05 mole of $Zn(NO_3)_2\cdot 6H_2O$ and 0.4 mole of 2-MIM were dissolved in 40 mL methanol and sonicated for 20 minutes, followed by stirring for 21 hours at room temperature. The obtained precipitate was washed with methanol and centrifuged.

The electrochemical experiments were carried out using a four-electrode bi-potentiostat (PARSTAT PMC 1000/1500 electrochemical workstation with the PINE INSTRUMENTS rotator) in a custom-made electrochemical cell. The catalytic ink was prepared from the 5 mg sample with 150 μL of isopropanol, 150 μL of Millipore water and 50 μL of Nafion (binder) mixture, as reported in our recent studies.[38] The uniformly dispersed catalytic ink was coated on a 5.6 mm glassy carbon (GC) disk of the rotating ring (Pt)-disk (GC) electrode (RRDE) with a theoretical collection efficiency of 0.37 (model: E7R9 RRDE tips). Previously, the electrode was polished with various grades of alumina slurry to mirror-finish and the particles were removed by ultrasonication. The catalytic ink (6.9 μL) was drop-coated on the GC disk of the RRDE, and the loading density of the catalyst was 0.4 mg cm^{-2}. Finally, the electrode was dried under a N_2 atmosphere. The Ag/AgCl (sat. KCl) and carbon cloth with a graphite rod were used as the reference and counter electrodes. The potentials were corrected to a reversible hydrogen electrode from the pH of the electrolyte. The linear sweep voltammetry (LSV) experiment was performed by scanning the potential from 1.2 to 0.1 V in an O_2-saturated 0.1 M KOH electrolyte. The blank experiment was conducted to subtract the charging current in the N_2-saturated electrolyte. During the ORR measurement, the ring electrode was kept at a constant potential (0.25 V) to oxidise the H_2O_2 intermediate formed on the disc. The number of electrons and percentage of H_2O_2 were calculated using the reported equations (ESI†). The OER was evaluated using the rotating disk electrode voltammetry in 1 M KOH electrolyte.

A self-made aqueous zinc–air battery was assembled using CF10-N/C4 catalyst coated (loading density is 1 mg cm^{-2}) air electrode, as described in previous work.[39,40] The carbon paper (Toray) was used as an air electrode, and the zinc plate (0.5 mm thickness) was used as the anode. The electrolyte is a mixture of KOH (6 M) and $Zn(CH_3COO)_2$ (0.2 M) solution. The air-accessible surface area of the air electrode is 1.539 cm^2.

Results and discussion

The ZIF-8 and $CoFe_2O_4$ materials are separately characterised by XRD patterns, and the synthesised ZIF-8 in the presence of $CoFe_2O_4$ ($CoFe_2O_4$ encapsulated ZIF-8) has a similar XRD pattern, which may be due to the highly crystalline and larger quantity of ZIF-8 compared with the $CoFe_2O_4$ (Fig. S1†). Subsequent pyrolysis of the composite at 900 °C leads to the decomposition of the ZIF-8, followed by the formation of the graphitisation. Interestingly, the new peaks in the XRD pattern

Paper

after pyrolysis indicate the CoFe alloy formation (Fig. 1a). The ZIF-8 provides the carbon and nitrogen source for graphitisation, leading to the N-doped carbon. The pyrolysis time was optimised where the XRD pattern demonstrates the presence of both the CoFe alloy and $CoFe_2O_4$ (Fig. S2†) after four hours of pyrolysis. During the high temperature pyrolysis, the metallic zinc forms and evaporates at ~900 °C. The evaporation of Zn after the graphitisation created the pores, producing the porous N-doped carbon material. The increasing content of $CoFe_2O_4$ in the initial composite material leads to the disappearance of $CoFe_2O_4$ peaks due to the thick formation of graphitic layers catalysed by the CoFe alloy, which hinders the exposure of $CoFe_2O_4$ particles. Fig. 1b shows the Raman spectra of synthesised materials. The defect density was estimated using the I_D/I_G value and was 1.21 for N/C4 catalysts. Incorporating $CoFe_2O_4$ induces more graphitisation, resulting in a decrease in the I_D/I_G value.[41] The value is not decreased while increasing the $CoFe_2O_4$ content beyond 10 wt% in the initial mixture.

The SEM images of synthesised materials are shown in Fig. 1c–f. The bare N/C4 shows a highly porous morphology, as reported in the literature (Fig. 1c). However, the $CoFe_2O_4$ incorporated carbon (CF10–N/C4) leads to fibril structures on the top of the porous N-doped carbon particles (like core–corona morphology), as shown in Fig. 1d. Upon increasing the $CoFe_2O_4$ content, bulk porous structures were seen significantly, with occasional fibril structures (Fig. 1e and f). This may

be attributed to the decreasing carbon content to the metal ratio, further confirmed by energy-dispersive X-ray analysis (EDAX) (Fig. S3†). The $CoFe_2O_4$–N-doped porous carbon composite was further analysed using transmission electron microscopy (TEM), as shown in Fig. 2a and b. The TEM images reveal that the fibril structure corresponds to the N-doped carbon nanotubes (N-CNT), whose average diameter is 50 nm. The length of the nanotubes varies from a few hundred nanometers to a few micrometres. The high-angle annular dark-field scanning transmission electron microscopic (HAADF-STEM) images indicate the presence of Co and Fe, some of which are present at the edges of the nanotubes. The selected area electron diffraction (SAED) pattern from the metal nanoparticles and its lattice fringes indicate that the d-spacing was estimated to be 0.21 nm, matching the 110 plane of the CoFe alloy (Fig. 2c and d). This strongly suggests that the CoFe alloy was formed during the pyrolysis, catalysing the N-CNT formation. Further, the electron energy loss spectroscopy (EELS) elemental mapping of the compound shows that metals were present in the bulk region along with carbon and nitrogen as shown in Fig. 2f–l. This indicates that Co and Fe were wrapped with graphitic layers derived from ZIF-8. The nanotubes comprised carbon and nitrogen, and no metallic traces were present on the tube. A trace amount of Zn was also observed due to the ZIF-8 precursor.

The compounds were characterised using X-ray photoelectron spectroscopy (XPS) to analyse the nature of the atomic species, as shown in Fig. 3. The C-1s spectra indicate that the carbon is present in the form of sp^2–C (284.3 eV), sp^3–C (285.3 eV), C–N (286.4 eV), C–O (288 eV) and C=O (290 eV) (Fig. S4a†). Similarly, O-1s spectra were deconvoluted into many peaks; among them, the peaks at 528.9 and 529.6 eV are attributed to the oxygen in the crystal lattice. The peaks at 530.4, 531.6, 532.2, and 533.2 eV referred to the different oxygen functional groups in the graphitic carbon (Fig. S4b†). The N-1s spectra (Fig. 3a) reveal that the nitrogen was present in its typical forms, such as pyridinic (398.1 eV), pyrrolic (399.6 eV), graphitic (401 eV) and nitrogen oxides (403.5 eV). The pyridinic and pyrrolic forms of nitrogen are present in major portions, which play crucial roles in the ORR activity.[42,43] The XPS peaks of Fe and Co species in the composite materials were analysed, and the Co and Fe contents were observed as 0.43% and 0.62% from the survey spectrum. These values correspond to the surface concentrations of Co and Fe whereas the bulk concentrations are much higher than the surface content, which is analysed later. The deconvoluted Fe-2p XPS peaks confirm the metallic Fe (706.4 eV) as a major portion, followed by the Fe^{2+} and Fe^{3+} in equal amounts (Fig. 3b). $Co-2p_{3/2}$ and $Co-2p_{1/2}$ were deconvoluted, and the major peak at 777.4 eV refers to the metallic cobalt (Fig. 3c). The other peaks refer to the higher oxidation states of cobalt (Co^{2+} and Co^{3+}). Similarly, the significant amount of the metallic cobalt and iron in the sample confirms the formation of the CoFe alloy, which has already been confirmed by the intense 110 peak (44.8°) in the powder XRD pattern.

The metal content was estimated using the thermogravimetric analysis (TGA), as shown in Fig. 3d. The materials were heated in the air atmosphere to remove the carbon content. A
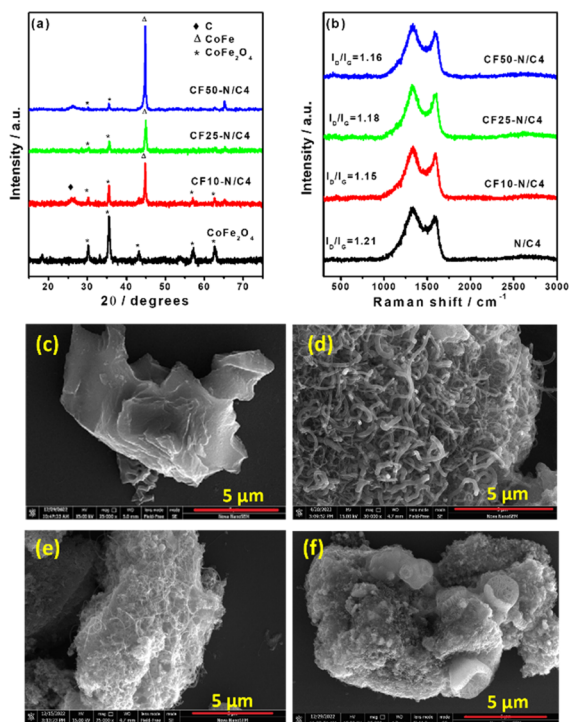

Fig. 1 (a) The PXRD patterns of $CoFe_2O_4$ and $CoFe_2O_4$-containing N-doped porous carbon materials of different $CoFe_2O_4$ contents. (b) The Raman spectra of the above said materials with and without $CoFe_2O_4$. The SEM images of (c) metal-free N-doped porous carbon materials (N/C4). Core–corona structured (d) CF10–N/C4 and (e) CF25–N/C4 materials. (f) Bulk porous CF50–N/C4 image.
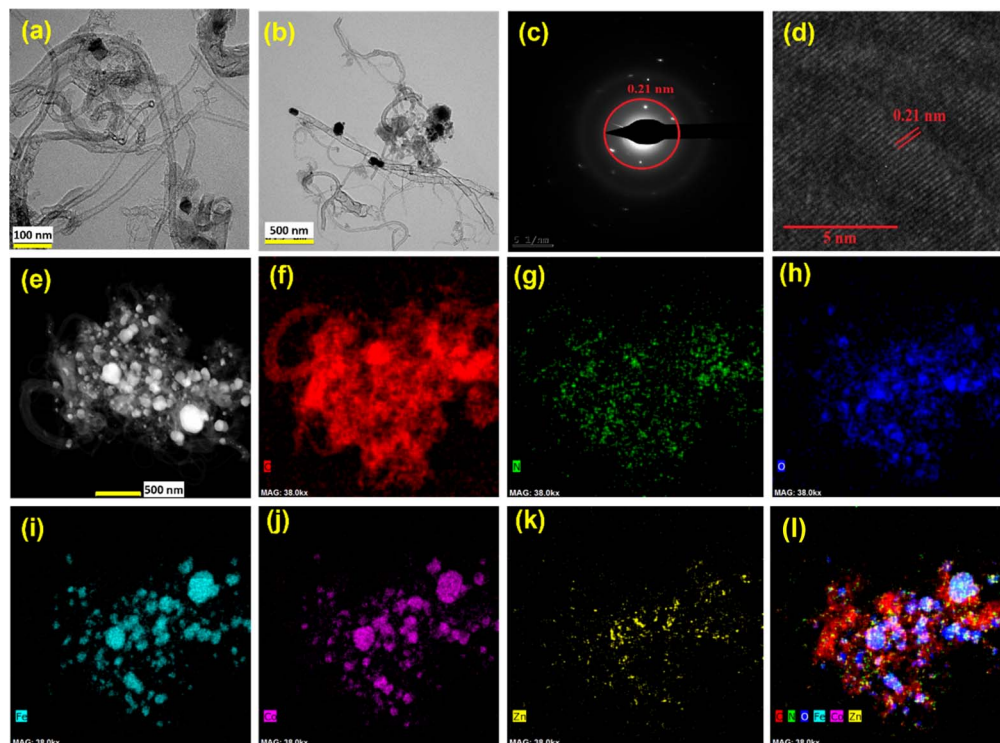
Fig. 2 (a) and (b) HR-TEM images of CF10−N/C4. (c) SAED pattern of CF10−N/C4. (d) The lattice fringes with a d spacing value of 0.21 nm, corresponding to the 110 plane of the CoFe alloy. (e) HAADF image of CF10−N/C4 and the EELS elemental mapping of (f) carbon, (g) nitrogen, (h) oxygen, (i) iron, (j) cobalt and (k) zinc. (l) Overlay of all elements present in CF10−N/C4.

significant weight loss was observed above 400 °C, indicating the carbon matrix removal from the composite.[44] The left-over materials were analysed using XRD, indicating the $CoFe_2O_4$ structure (Fig. S5b†). The TGA of N/C4 (without $CoFe_2O_4$) shows 7.2 wt% of ZnO, the same for all the compounds. After the ZnO correction, the TGA curves indicate that the CF10−N/C4 and CF25−N/C4 samples have 9.7% and 23.2% $CoFe_2O_4$, respectively. The TGA curve of acid-washed CF10−N/C4 shows 2 wt% metal oxide content (Fig. S6†), and the EELS mapping confirms that the remaining material consists of oxides of Zn, Co and Fe (Fig. S7†).

The surface area and porosity of the materials were analysed using Brunauer–Emmett–Teller (BET) adsorption isotherms, demonstrating the Type IV adsorption (Fig. 3e). However, the materials consist of micropores predominantly due to the evaporation of zinc during the heat treatment.[29,45,46] The N/C4 (synthesised from ZIF-8 without $CoFe_2O_4$) exhibits the highest surface area (1004 m^2 g^{-1}), whereas the incorporation of $CoFe_2O_4$ decreases the surface area due to the formation of the bulk $CoFe_2O_4$ structure. Besides, it increases the slit narrow mesopores, demonstrated by the H4 hysteresis loop.[47] The non-local density functional theoretical (NLDFT) analysis reveals that CF10−N/C4 and CF25−N/C4 consist of narrow mesopores whose diameter varies from 2 to 3 nm (Fig. 3f). The role of micropores and narrow mesopores was discussed in the literature, and their presence is indispensable for carbon-based materials to improve ORR activity.[48] The surface area of CF50−N/C4 is small and consists of most mesopores.

The hydrodynamic rotating ring-disk electrode voltammograms of $CoFe_2O_4$ carbon composites are shown in Fig. 4a. The pyrolysis time was optimised to 4 hours for the best ORR activity. The CF10−N/C4 shows the highest positive onset (E_{onset} = 1.00 V) and half-wave potential ($E_{1/2}$ = 0.84 V), which is highest among all the composites synthesised with different loadings of $CoFe_2O_4$ and pyrolysis times. The E_{onset} and $E_{1/2}$ values are decreased while increasing the $CoFe_2O_4$ content, and it may be attributed to the decrease in the electrical conductivity of the catalysts, as shown in Table S2.† Among the materials studied in this work, CF10−N/C4 and CF25−N/C4 show better $E_{1/2}$ values (0.84 V and 0.81 V, respectively). The number of electrons was calculated from the ring and disk currents as 3.8 for CF10−N/C4 and CF25−N/C4, demonstrating the complete 4-electron reduction of the ORR (Fig. 4b). The $CoFe_2O_4$-free N/C4 catalysts show the lowest activity despite having a larger surface area, indicating the role of metals (Co and Fe) towards the ORR activity.[31] Table S3† shows the ORR activities of the similar materials studied in the literature.

A few control experiments were performed to understand the active sites of the materials (Fig. 4c and d). The role of metals was analysed by removing them using acid-washing. The CF10−N/C4 was washed with 0.1 M HCl overnight to remove the metal and metal oxides in the material. The acid-washed catalyst was referred to as CF10−N/C4−AW. The XRD confirms the removal of the CoFe alloy and $CoFe_2O_4$ particles, and only the 002 peak corresponding to the graphitic carbon is observed (Fig. S8†). Further, the compound was analysed using the TEM and EELS
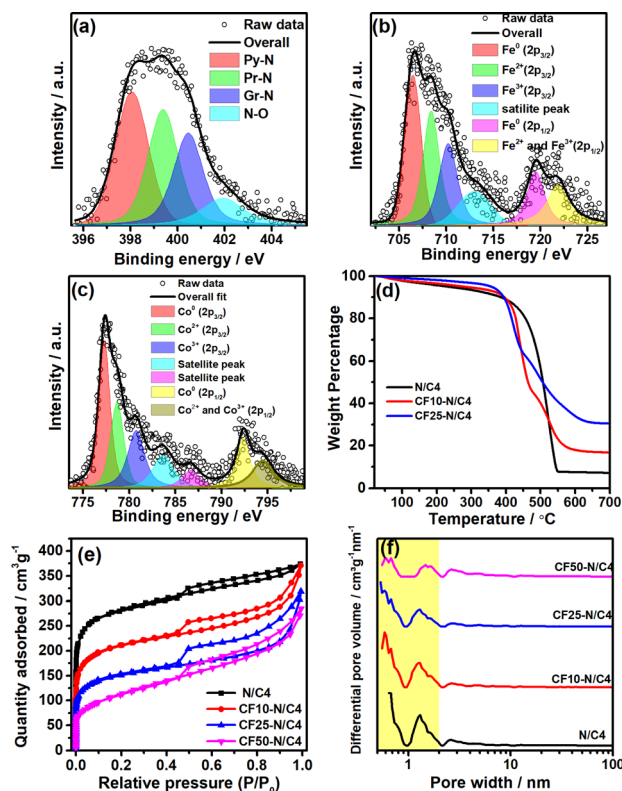
Fig. 3 (a) N-1s, (b) Fe-2p and (c) Co-2p XPS spectra of CF10−N/C4 and their deconvoluted peaks for their various chemical states. (d) The TGA of CF10−N/C4 and CF25−N/C4 in comparison with the N/C4 to estimate the quantity of zinc from ZIF-8. (e) BET adsorption isotherms and (f) their corresponding pore size analysis using the NL-DFT method.

Fig. 4 Linear sweep voltammogram of the ORR on $CoFe_2O_4$/N-doped carbon composites and the potential-dependent number of electrons (n). (a) RRDE voltammograms of CF−N/C compounds at various contents of initial $CoFe_2O_4$ and (b) its potential dependent n and % H_2O_2. (c) Comparison of RRDE voltammograms to study the role of the $CoFe_2O_4$ and CoFe alloy and its potential dependent n and % H_2O_2 (d). (e) RRDE voltammograms of controlled samples containing only Fe or Co oxide containing porous N-doped carbon and (f) potential dependent n and % H_2O_2 plots.

mapping (Fig. S7†). Although small metal traces are present in the acid-washed samples, these metallic species should be wrapped with the graphitic carbon layers. The nanotube morphology was retained after the acid washing (Fig. S12b†). The CF10−N/C4−AW shows the E_{onset} and n values of 0.95 V and 3.5, respectively, slightly lower than the CF10−N/C4. The decrease in the activity can be rationalised by removing the $CoFe_2O_4$ or CoFe alloy, indicating the vital role of the metal species (in the form of alloy). The accelerated durability test (ADT) was performed using the protocol proposed by DoE. The CF10−N/C4 shows only a 10 mV negative shift after 10 000 cycles, indicating excellent stability during the ORR (Fig. S9†).

Further, the origin of the ORR activity can be studied to discern the roles of $CoFe_2O_4$ and CoFe alloy species. The ORR activity of metal-free N/C4 exhibits lower E_{onset} and $E_{1/2}$ values (0.90 and >0.7 V) with a current density of 3 mA $^{-2}$. The physical mixture of $CoFe_2O_4$ with N/C4 (CFO + N/C4) can reveal the role of the CoFe alloy and $CoFe_2O_4$. One can effectively exclude the CoFe alloy contribution in the physical mixture, which forms during the heat treatment. The ORR activity of CFO + N/C4 is closely similar to that of the N/C4, demonstrating that the $CoFe_2O_4$ did not act as ORR active sites. Furthermore, the physical mixture of $CoFe_2O_4$ with CF10−N/C4−AW (CFO + CF10−N/C4−AW) does not regain the original activity of CF10−N/C4,
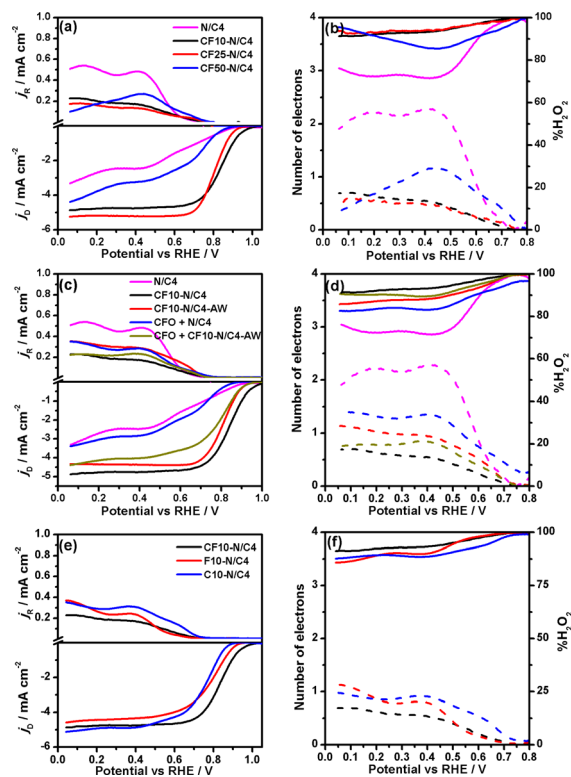
indicating that the acid-washed step removed the $CoFe_2O_4$, which did not involve in the ORR. Based on these studies, it was confirmed that the graphitic carbon encapsulated CoFe alloy should be the active site for the ORR.

To understand the role of individual atomic species in the CoFe alloy, the iron oxide + ZIF-8 and cobalt oxide + ZIF-8 composites were synthesised and pyrolysed separately, referred to as C10−N/C and F10−N/C materials (Fig. 4e and f). The XRD pattern indicates the combination of Fe_3O_4 and Fe metallic particles in the F10−N/C catalysts, whereas the C10−N/C catalyst shows only Co metallic nanoparticles (Fig. S10†). The SEM images of C10−N/C4 and F10−N/C4 catalysts reveal a highly porous morphology wherein the formation of the nanotubes (or core–corona structural motif) is not observed (Fig. S11†). The RRDE voltammograms of the C10−N/C4 and F10−N/C4 materials demonstrate that the ORR activities of both these materials are lower than that of CF10−N/C4 (E_{onset} = 0.95 and 0.91 for F10−N/C4 and C10−N/C4 catalysts, respectively), indicating that the encapsulated CoFe alloy, as a whole, acts as an active site for the ORR.

Bimetallic materials could be the best choice due to their bifunctional activity in the ZAB application. The OER activity of
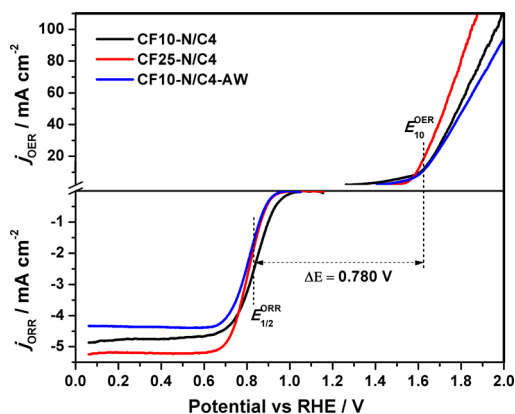
Fig. 5 Comparison of the linear sweep voltammograms of the ORR and OER regions of the CF–N/C4 materials at the rotational speed of 1600 rpm. The scan rate is 10 mV s⁻¹. The electrolytes are O₂-saturated 0.1 M KOH and 1 M KOH for ORR and OER measurements, respectively.

these materials is evaluated in the 1 M KOH electrolyte, as shown in Fig. 5. The E_{10} values (potential at which the current reaches 10 mA cm⁻²) indicate that the CF10–N/C4 (1.607 V), CF25–N/C4 (1.592 V) and CF10–N/C4–AW (1.616 V) materials are good OER catalysts. The acid-washed compound (CF10–N/C4–AW) shows a slight anodic shift. The potential difference between the ORR ($E_{1/2}$) and OER (E_{10}) is a measure of bifunctional catalyst activity, referred to as ΔE. The ΔE value of CF10–N/C4 and CF25–N/C4 catalysts was estimated to be 0.76 and 0.78 V, respectively, which are excellent values for a material to be a bifunctional catalyst. Hence, these materials can be used as oxygen electrocatalysts in rechargeable zinc–air battery applications.

An aqueous Zn–air battery was constructed using CF10–N/C4, CF25–N/C4 and CF10–N/C4–AW, as explained in the methodology section. The SEM images of the CF10–N/C4 coated carbon paper air electrode indicate the uniform distribution of the particles (Fig. S15a†). The open-circuit potential (E_{OCP}) was measured as 1.53 V for CF10–N/C4, followed by CF25–N/C4 (1.50 V) and CF10–N/C4–AW (1.50 V). The polarization curves

demonstrate that the power density of CF10–N/C4 and CF10–N/C4–AW is 159 mW cm⁻² (at 211 mA cm⁻²) and 162 mW cm⁻² (at 227 mA cm⁻²), respectively, as shown in Fig. 6a. A similar trend was observed with gravimetric energy density values (Fig. S13†). Almost similar power density values were observed for CF10–N/C4 and CF10–N/C4–AW, indicating that the metal content outside the graphitic layer is not primarily involved in the activity. In contrast, the activity is enhanced by the encapsulated CoFe alloy. The increasing CoFe₂O₄ creates a negative impact on the overall efficiency. The specific capacity at the constant discharge current density of 20 mA cm⁻² was estimated as 900 mA h g$_{Zn}$⁻¹ for CF10–N/C4–AW, whereas the other two compounds exhibit lower specific capacities (Fig. 6b). These values demonstrate that a small portion could be the active site in the composite, where the CoFe plays an essential role in enhancing the activity. The galvanostatic charge–discharge experiment was performed with a charging density of 5 mA cm⁻² and 20 minutes per cycle. The catalysts are stable until 45 hours of operation (120 cycles), wherein no change was observed in the charge and discharge potential (Fig. S14†). The longer the number of cycles, the lower the cell performance, which may be attributed to the carbon corrosion at higher positive potentials. This was further confirmed by the SEM analysis of the carbon air electrode, indicating the formation of porous carbon bulky particles with fewer carbon nanotubes on the surface of the particles (Fig. S15b†). Further, the catalyst was analysed using the XPS technique after the galvanostatic charge–discharge tests. Besides the typical elements present in the CF10–N/C4, potassium (K-2p, 295.9 eV), fluorine (F-1s, 689.0 eV), sulphur (S-2p, 170.5 eV) and zinc (Zn-2p$_{3/2}$, 1023.5 eV) were found in larger portions in the survey spectrum. The presence of these elements (K, F, S and Zn) may be attributed to the KOH electrolyte, Nafion (tetrafluoroethylene sulphonic acid polymer) binder and zinc oxide (from anode). Traces of Co and Fe were found and deconvoluted to study the oxidation states. The Co⁰ and Fe⁰ (encapsulated with thinner carbon layers) peaks indicates the presence of the CoFe alloy in the catalyst layer (Fig. S16†), which is lower than the amount of CoFe estimated
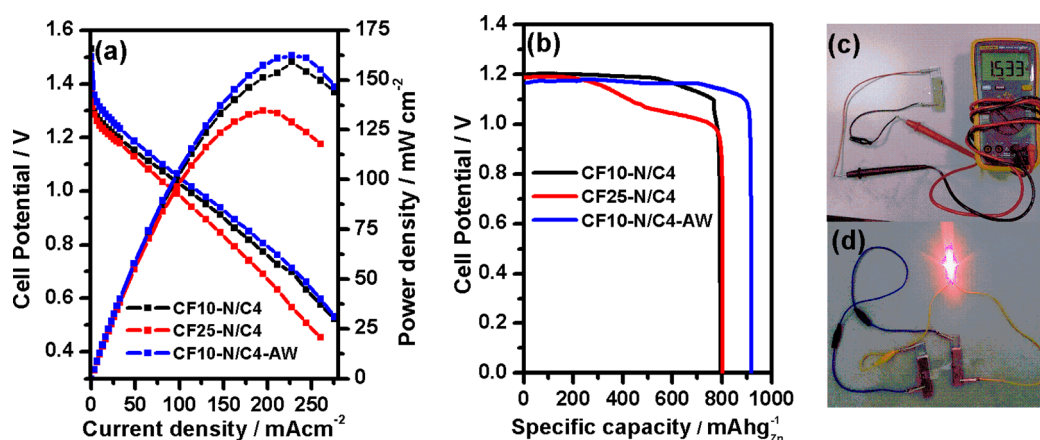

Fig. 6 (a) Polarisation curves of the zinc–air battery tested with CF–N/C composites. (b) Specific capacity plots at the discharge current density of 20 mA cm⁻². The pictures showing the (c) OCP and (d) glowing LED light application using the solid-state zinc–air battery.

before the zinc–air battery testing. A comparative study of the zinc–air battery performances using similar materials is given in Table S4.†

The solid-state zinc–air battery experiment was performed using the gel electrolyte prepared from polyvinyl alcohol (PVA) and KOH,[49] as shown in Fig. 6c and d. The E_{OCP} was measured as 1.53 V for CF10–N/C4, close to that of the benchmark Pt/C + RuO$_2$ catalysts (1.56 V). The power density value was calculated as 22.4 mW cm^{-2} (Fig. S17†), and the galvanostatic charge–discharge test (for 1 mA cm^{-2} current density) exhibits cycling stability comparable with that of the Pt/C + RuO$_2$ catalysts (Fig. S18†).

Conclusions

Porous CoFe$_2$O$_4$-containing nitrogen-doped carbon was synthesised from ZIF-8 and CoFe$_2$O$_4$ for use as oxygen electrocatalysts in the zinc–air battery electrode. The CoFe$_2$O$_4$ incorporation increases the graphitisation and produces carbon nanotubes on the surface of porous N-doped carbon particles (core–corona structure). Despite having the higher surface area of metal-free porous nitrogen-doped carbon (from ZIF-8), the metal-containing (Co and Fe) CF10–N/C4 exhibits much higher ORR and OER activity, which is comparable to those of the benchmark Pt/C (ORR) and RuO$_2$ (OER) catalysts. The formation of the CoFe alloy was confirmed using the spectroscopic techniques, and the control experiments indicate that CoFe alloy particles are the main active sites for the ORR activity along with N-doped carbon. Besides, the OER activity is also improved due to the CoFe alloy, indicating the excellent bifunctional activity of the CoFe alloy. The liquid electrolyte zinc–air battery exhibits excellent power density and specific capacity, and the solid-state zinc–air battery was demonstrated to show the real-time application.

Author contributions

SB performed synthesis and electrochemical analysis and drafted the manuscript. EAA performed the liquid and solid-state battery experiments. AM conceptualised, supervised the work and finalised the manuscript.

Conflicts of interest

There are no conflicts to declare.

Acknowledgements

Notes and references

1 J.-S. Lee, S. Tai Kim, R. Cao, N.-S. Choi, M. Liu, K. T. Lee and J. Cho, *Adv. Energy Mater.*, 2011, **1**, 34–50.

2 J. Fu, Z. P. Cano, M. G. Park, A. Yu, M. Fowler and Z. Chen, *Adv. Mater.*, 2017, **29**, 1604685.

3 A. Iqbal, O. M. El-Kadri and N. M. Hamdan, *J. Energy Storage*, 2023, **62**, 106926.

4 R. Zhao, Q. Li, X. Jiang, S. Huang, G. Fu and J.-M. Lee, *Mater. Chem. Front.*, 2021, **5**, 1033–1059.

5 W. T. Hong, M. Risch, K. A. Stoerzinger, A. Grimaud, J. Suntivich and Y. Shao-Horn, *Energy Environ. Sci.*, 2015, **8**, 1404–1427.

6 S. Dresp, F. Luo, R. Schmack, S. Kühl, M. Gliech and P. Strasser, *Energy Environ. Sci.*, 2016, **9**, 2020–2024.

7 K. Tang, H. Hu, Y. Xiong, L. Chen, J. Zhang, C. Yuan and M. Wu, *Angew. Chem., Int. Ed.*, 2022, **61**, e202202671.

8 K. Tang, C. Yuan, Y. Xiong, H. Hu and M. Wu, *Appl. Catal., B*, 2020, **260**, 118209.

9 R. Na, K. Min, H. Kim, Y. Son, S. E. Shim and S.-H. Baeck, *J. Energy Chem.*, 2023, **84**, 140–152.

10 R. S. Kumar, S. Prabhakaran, S. Ramakrishnan, S. C. Karthikeyan, A. R. Kim, D. H. Kim and D. J. Yoo, *Small*, 2023, **19**, 2207096.

11 J. Wang, C.-X. Zhao, J.-N. Liu, D. Ren, X. Ma, B.-Q. Li, J.-Q. Huang and Q. Zhang, *Particuology*, 2023, **77**, 146–152.

12 B. Ricciardi, W. da Silva Freitas, B. Mecheri, K. U. Nisa, J. Montero, V. C. A. Ficca, E. Placidi, C. Alegre and A. D'Epifanio, *Carbon*, 2024, **219**, 118781.

13 S. Ren, X. Duan, S. Liang, M. Zhang and H. Zheng, *J. Mater. Chem. A*, 2020, **8**, 6144–6182.

14 Y.-j. Wu, X.-h. Wu, T.-x. Tu, P.-f. Zhang, J.-t. Li, Y. Zhou, L. Huang and S.-g. Sun, *Appl. Catal., B*, 2020, **278**, 119259.

15 D. Xie, D. Yu, Y. Hao, S. Han, G. Li, X. Wu, F. Hu, L. Li, H.-Y. Chen, Y.-F. Liao and S. Peng, *Small*, 2021, **17**, 2007239.

16 M. Mechili, C. Vaitsis, N. Argirusis, P. K. Pandis, G. Sourkouni and C. Argirusis, *Renewable Sustainable Energy Rev.*, 2022, **156**, 111970.

17 Y. Kumar, M. Mooste and K. Tammeveski, *Curr. Opin. Electrochem.*, 2023, **38**, 101229.

18 E. Davari and D. G. Ivey, *Sustainable Energy Fuels*, 2018, **2**, 39–67.

19 G. Janani, Y. Chae, S. Surendran, Y. Sim, W. Park, J. K. Kim and U. Sim, *Appl. Sci.*, 2020, **10**, 3165.

20 Q. Zhao, Z. Yan, C. Chen and J. Chen, *Chem. Rev.*, 2017, **117**, 10121–10211.

21 S. Jha, P. Jain, R. Palkovits and P. Popinand Ingole, *J. Mater. Chem. A*, 2023, **11**, 23034–23047.

22 L.-L. Liu, D.-H. Wu, L. Zhang, J.-J. Feng and A.-J. Wang, *J. Colloid Interface Sci.*, 2023, **639**, 424–433.

23 Y. Sun, J. Wang, Q. Liu, M. Xia, Y. Tang, F. Gao, Y. Hou, J. Tse and Y. Zhao, *J. Mater. Chem. A*, 2019, **7**, 27175–27185.

24 L. Liu, Z. Xu, T. Lu, Z. Wang, X. Shi, C. Li, Y. Wei and Z. Zi, *J. Alloys Compd.*, 2022, **906**, 164296.

25 A. Samanta and C. R. Raj, *J. Phys. Chem. C*, 2018, **122**, 15843–15852.

26 J. M. Gonçalves, M. I. da Silva, M. N. T. Silva, P. R. Martins, E. Nossol, H. E. Toma and L. Angnes, *Energy Adv.*, 2022, **1**, 793–841.

27 Y. Song, C. Yu, D. Ma and K. Liu, *Coord. Chem. Rev.*, 2024, **499**, 215492.

28 J. Liu, Y. Xie, Y. Nan, G. Gou, X. Li, Y. Fang, X. Wang, Y. Tang, H. Yang and J. Ma, *Electrochim. Acta*, 2017, **257**, 233–242.

29 H.-X. Zhong, J. Wang, Y.-w. Zhang, W.-l. Xu, W. Xing, D. Xu, Y.-f. Zhang and X.-b. Zhang, *Angew. Chem., Int. Ed.*, 2014, **53**, 14235–14239.

30 R. R. Salunkhe, Y. Kamachi, N. L. Torad, S. M. Hwang, Z. Sun, S. X. Dou, J. H. Kim and Y. Yamauchi, *J. Mater. Chem. A*, 2014, **2**, 19848–19854.

31 M. Jiang, X. Cao, D. Zhu, Y. Duan and J. Zhang, *Electrochim. Acta*, 2016, **196**, 699–707.

32 M. S. Matseke, H. Zheng and Y. Wang, *Appl. Surf. Sci.*, 2020, **516**, 146105.

33 X. Li, Y. Zhao, L. Ding, D. Wang, Q. Guo, Z. Li, H. Luo, D. Zhang and Y. Yu, *Nanomaterials*, 2021, **11**, 1088.

34 H. Wang, C. Liu, X. Yang, J. Gu, M. Niu, L. Yang and Z. Bai, *Int. J. Hydrogen Energy*, 2022, **47**, 6059–6066.

35 Y. Go, K. Min, H. An, K. Kim, S. Eun Shim and S.-H. Baeck, *Chem. Eng. J.*, 2022, **448**, 137665.

36 L. Gan, S. Shang, C. W. M. Yuen, S.-x. Jiang and E. Hu, *Appl. Surf. Sci.*, 2015, **351**, 140–147.

37 E. L. Bustamante, J. L. Fernández and J. M. Zamaro, *J. Colloid Interface Sci.*, 2014, **424**, 37–43.

38 J. Anjana and A. Muthukrishnan, *Catal. Sci. Technol.*, 2022, **12**, 6246–6255.

39 A. N. Eledath, A. Edathiparambil Poulose and A. Muthukrishnan, *ACS Appl. Eng. Mater.*, 2023, **1**, 2304–2314.

40 A. N. Eledath, A. E. Poulose and A. Muthukrishnan, *ACS Appl. Nano Mater.*, 2022, **5**, 10528–10536.

41 Y. Lu, Z. Zhu and Z. Liu, *Carbon*, 2005, **43**, 369–374.

42 H. Ji, M. Wang, S. Liu, H. Sun, J. Liu, T. Qian and C. Yan, *Electrochim. Acta*, 2020, **334**, 135562.

43 S. K. Singh, K. Takeyasu and J. Nakamura, *Adv. Mater.*, 2019, **31**, 1804297.

44 S. Arya Gopal, A. Edathiparambil Poulose, C. Sudakar and A. Muthukrishnan, *ACS Appl. Mater. Interfaces*, 2021, **13**, 44195–44206.

45 W. Chaikittisilp, M. Hu, H. Wang, H.-S. Huang, T. Fujita, K. C. W. Wu, L.-C. Chen, Y. Yamauchi and K. Ariga, *Chem. Commun.*, 2012, **48**, 7259–7261.

46 J. Hernández-Ferrer, M. Gracia-Martín, A. M. Benito, W. K. Maser and E. García-Bordejé, *Catal. Today*, 2023, **423**, 113993.

47 H. Qutaish, J. Lee, Y. Hyeon, S. A. Han, I.-H. Lee, Y.-U. Heo, D. Whang, J. Moon, M.-S. Park and J. H. Kim, *Appl. Surf. Sci.*, 2021, **547**, 149134.

48 J. Anjana, A. N. Eledath and A. Muthukrishnan, *Mater. Adv.*, 2023, **4**, 4216–4225.

49 L. Wang, M. Xu, H. Li, Z. Huang, L. Wang, T. Taylor Isimjan and X. Yang, *Inorg. Chem.*, 2023, **62**, 13284–13292.